

3D Gap Opening in Non-Ideal MHD Protoplanetary Disks: Asymmetric Accretion, Meridional Vortices, and Observational Signatures

Xiao Hu (胡晓)^{1,2*}, Zhi-Yun Li², Jaehan Bae¹, Zhaohuan Zhu (朱照寰)^{3,4}

¹*Department of Astronomy, University of Florida, Gainesville, FL 32608, USA*

²*Department of Astronomy, University of Virginia, Charlottesville, VA 22904, USA*

³*Department of Physics and Astronomy, University of Nevada, Las Vegas, 4505 S. Maryland Parkway, Las Vegas, NV 89154, USA*

⁴*Nevada Center for Astrophysics, University of Nevada, Las Vegas, 4505 South Maryland Parkway, Las Vegas, NV 89154, USA*

Accepted XXX. Received YYY; in original form ZZZ

ABSTRACT

Recent high-angular resolution ALMA observations have revealed rich information about protoplanetary disks, including ubiquitous substructures and three-dimensional gas kinematics at different emission layers. One interpretation of these observations is embedded planets. Previous 3-D planet-disk interaction studies are either based on viscous simulations, or non-ideal magnetohydrodynamics (MHD) simulations with simple prescribed magnetic diffusivities. This study investigates the dynamics of gap formation in 3-D non-ideal MHD disks using non-ideal MHD coefficients from the look-up table that is self-consistently calculated based on the thermo-chemical code. We find a concentration of the poloidal magnetic flux in the planet-opened gap (in agreement with previous work) and enhanced field-matter coupling due to gas depletion, which together enable efficient magnetic braking of the gap material, driving a fast accretion layer significantly displaced from the disk midplane. The fast accretion helps deplete the gap further and is expected to negatively impact the planet growth. It also affects the corotation torque by shrinking the region of horseshoe orbits on the trailing side of the planet. Together with the magnetically driven disk wind, the fast accretion layer generates a large, persistent meridional vortex in the gap, which breaks the mirror symmetry of gas kinematics between the top and bottom disk surfaces. Finally, by studying the kinematics at the emission surfaces, we discuss the implications of planets in realistic non-ideal MHD disks on kinematics observations.

Key words: accretion, accretion disks — magnetohydrodynamics (MHD) — planets and satellites: formation — circumstellar matter — method: numerical

1 INTRODUCTION

Recent observations indicate that protoplanetary disks ubiquitously exhibit substructures (e.g., [ALMA Partnership et al. 2015](#); [Huang et al. 2018](#); [Andrews 2020](#)), including rings and gaps, which are present in both gas and dust components ([Bae et al. 2023](#)). Numerous theoretical models have been developed to explain these features. Inherent physico-chemical processes within the disk, such as the sublimation fronts of different volatile, i.e., snow lines, can influence dust growth and thereby lead to the formation of rings and gaps ([Zhang et al. 2015](#); [Okuzumi et al. 2016](#)). Interactions between dust and gas, such as direct aerodynamic drag (e.g., [Gonzalez et al. 2017](#)), and indirect effects from non-ideal

MHD processes ([Hu et al. 2019, 2021](#)), can also affect local accretion rates, giving rise to substructures. On the other hand, a popular explanation posits that these rings and gaps are indicative of young planets in formation (see the PPvii review by [Bae et al. 2023](#)).

High-resolution observations of molecular line emissions have uncovered more detailed gas structures within protoplanetary disks (e.g., [Teague et al. 2019](#); [Pinte et al. 2020](#)). Encouragingly, the substructures' azimuthal velocities closely match the perturbations caused by planets, supporting the increasingly accepted hypothesis of gap opening by massive planets. On the other hand, radial and vertical velocities exhibit considerably complex structures. The Molecules with ALMA at Planet-forming Scales (MAPS) ([Öberg et al. 2021](#)) survey conducted spatial mapping of multiple chemical species across five protoplanetary disks:

* E-mail: xiao.hu.astro@gmail.com

MWC 480, HD 163296, AS 209, IM Lup, and GM Aur. Notably, the vertical velocities near the gaps in HD163296 and AS209 (Izquierdo et al. 2023; Galloway-Sprietsma et al. 2023) do not align with the collapsing flows predicted by hydrodynamic simulations (Kley et al. 2001; Fung & Chiang 2016), casting doubts on the planet-disk interaction interpretation.

Gap opening in protoplanetary disks by planets is a classic problem in planet formation, wherein the planet’s gravity launches spiral density waves, depositing significant torque in the disk (e.g., Lin & Papaloizou 1993). This torque alters the disk structure, resulting in a local low-density annulus (i.e., a planetary gap) along the planetary orbit, influencing gas and solids accretion as well as orbital migration of the planet (e.g., Crida et al. 2006; Baruteau et al. 2014). While early studies have been carried out adopting hydrodynamic, viscous disks, recent studies have shown that the accretion and angular momentum transport in protoplanetary disks are governed by magnetically-driven disk winds (e.g., Béthune et al. 2017; Wang et al. 2019). Some previous hydrodynamical simulations have introduced wind torque to approximate the effects of wind-driven accretion in disks. Even in simplified one-dimensional models, such as those by Ogiwara et al. (2015, 2017), quite intriguing results have been found regarding the migration of low-mass planets: the inward migrational torque is weakened, and can even be reversed. In two-dimensional simulations, Kimmig et al. (2020) found that the migration of massive planets could also reverse under certain conditions. Lega et al. (2022) and Elbakyan et al. (2022) pointed out more complex behaviors, such as the ease of vortex formation at the edge of the gap by wind-driven accretion, and a reduction in the timescale for gap opening, both of which can influence the rate of planet migration and the criteria for gap opening mass. Tabone et al. (2022) employ a parameter similar to the viscous α , denoted as α_{dw} , to evaluate the wind loss rate in one-dimensional model, facilitating the study of the long-term evolution of wind-driven accretion disks.

While these hydro models have made significant progress using simplified disk wind treatment, it is widely recognized that magnetic fields play a crucial role in both launching disk winds and the corresponding angular momentum transfer processes. Magnetic fields have been shown to play important roles in carving gaps by direct surface accretion stream (Suriano et al. 2017) or radial magnetic flux redistribution (e.g., Suriano et al. 2018; Hu et al. 2019, 2021; Cui & Bai 2021). In turn, the spiral wakes and gaps generated by planets should also affect the distribution of magnetic fields. The wind torque and wind loss rate are intricately linked to the disk’s magnetization, determined by its surface density and the strength of the poloidal magnetic field (Riols et al. 2020; Lesur 2021). Their dynamical importance motivated numerical studies that combine planet-disk interaction with magnetic fields and wind-driven accretion. Early simulations along this line usually assumed ideal MHD and incorporated only a toroidal magnetic field without launching a disk wind (Nelson & Papaloizou 2003; Winters et al. 2003; Baruteau et al. 2011). More recent local shearing-box MHD simulations have included a net poloidal magnetic flux and found that the magnetic flux gets concentrated into the planet-induced gap, making the gap deeper and wider due to enhanced magneto-rotational instability

(MRI) turbulence within the gap (Zhu et al. 2013; Carballido et al. 2017). However, besides being local, these studies are typically unstratified in the vertical direction and thus incapable of wind-driven angular momentum transport.

Once magnetic fields are considered, non-ideal MHD processes become crucial, as outer protoplanetary disks are weakly ionized. Gressel et al. (2013) included Ohmic dissipation in a global simulation, but its extent is limited to 4.5 disk scale heights, limiting the disk wind’s treatment. Aoyama & Bai (2023) conducted three-dimensional global non-ideal magneto-hydrodynamic simulations with ambipolar diffusion to investigate Type-II planet-disk interactions. Their findings highlighted how embedded planets could lead to a concentration of poloidal magnetic flux around their orbits, enhancing angular momentum removal and deepening the planetary gaps formed. This work emphasizes the crucial influence of magnetic fields and MHD winds on gap formation and planetary migration. Similarly, Wafflard-Fernandez & Lesur (2023) explored the dynamics of planet-disk interactions through high-resolution 3D global non-ideal MHD simulations, examining the effects of various planet masses and disk magnetizations on gap opening and meridional flows. Their research pointed to the significant impact of MHD winds on shaping disk structures and influencing the migration of embedded planets, reinforcing the importance of incorporating magnetic fields into models of planet formation and disk evolution.

However, these studies employed a simplified approach to magnetic diffusion, using a fixed profile for the ambipolar Elsasser number (Am), which may not capture the full complexity of magnetic interactions within protoplanetary disks. As the gas density changes due to the development of MHD winds, the ionization structure of the disk also changes which in turn affects the efficiency of the coupling between the magnetic fields and the gas. It is thus expected that the dimensionless Elsasser number, characterizing the diffusion timescale normalized by the local orbital period in protoplanetary disks would have spatial and temporal variations. Capturing this variation more self-consistently based on the recent thermochemical calculation (including ionization) of Hu et al. (2023) is a major goal of our investigation.

The paper is organized as follows. In §2, we describe the numerical methods and simulation setup. §3 analyzes the results from our simulation, focusing on the gas dynamics and the corresponding observational signatures. We discuss our results and conclude in §4.

2 METHODS

2.1 Disk

We simulate the non-ideal MHD disk evolution using *Athena++* (Stone et al. 2020). To minimize the grid noise of Keplerian rotation and the radially flowing disk wind, we perform simulation in spherical polar coordinates (r, θ, ϕ). The radial grid in our simulation is set from $r = 2$ to 100 in code units with logarithmic grid spacing. The θ grid extends from 0.05 to $\pi - 0.05$. The azimuthal ϕ grid spans from 0 to 2π . The root grid has 64, 48, and 96 cells in r, θ , and ϕ directions, respectively. We used 4 levels of static mesh refinement. The first 2 levels are axisymmetric, covering the

whole gap region, within $4 < r < 23$ and $\theta_{\text{mid}} < 0.5$ rad, where θ_{mid} is the angle above and below the midplane. The 3rd and 4th levels only cover the planet's vicinity, giving a resolution of 16 cells per scale height at the finest level. We use a corotating frame centered on the planet (Aoyama & Bai 2023) so the static mesh refinement can follow the circumplanetary disk region.

The disk midplane's initial density and temperature profile follow power-law functions with indices of p and q , respectively. The midplane density at $r = 1$ is set to unity in code units. The initial disk profile for density and temperature at the midplane is therefore:

$$\rho(R, z = 0) = \rho(R_0, z = 0) \left(\frac{R}{R_0} \right)^p \quad (1)$$

$$T(R, z = 0) = T(R_0, z = 0) \left(\frac{R}{R_0} \right)^q \quad (2)$$

We adopt $p = -2.2218$ and $q = -0.57$ to match the disk profile in Hu et al. (2023), and here $R = r \sin \theta$, $z = r \cos \theta$ are cylindrical coordinates. The entire temperature structure is adopted from a smooth disk (i.e., no-planet torque) run from Hu et al. (2023), and the temperature for each cell is calculated using bilinear interpolation in the meridian plane. In general, the disk is vertically isothermal within four scale heights above the midplane. Beyond this, the temperature increases by 50% within one additional scale height and then doubles at ten scale heights. The temperature of the corona continues to rise at higher altitudes, eventually plateauing at 2000-3000 K. This gives a midplane aspect ratio of 0.058 at $R=10$, and 0.035 at $R=1$, corresponding to $T=82$ K and 305 K when the code length unit equals 1 au. The disk is vertically isothermal with a hot corona. We use instant cooling to maintain a fixed temperature profile throughout the simulation. For the vertical density structure, the initial profile is calculated by assuming hydrostatic equilibrium in the $R - z$ plane, i.e., $v_R = v_z = 0$. As in Hu et al. (2023), the disk is initially threaded by a large-scale poloidal magnetic field, with a midplane plasma β (defined as the ratio between thermal pressure and magnetic pressure $\beta \equiv 2P_{\text{gas}}/B^2$) of 10^4 . The corresponding initial vector potential is adopted from Zanni et al. (2007):

$$A_\phi(r, \theta) = \frac{2B_{z0}R_0}{4+p+q} \left(\frac{r \sin \theta}{r_0} \right)^{\frac{p+q}{2}+1} [1 + (m \tan \theta)^{-2}]^{-\frac{5}{8}} \quad (3)$$

where p , q and r_0 are from Eq.1,2, and m is a parameter that specifies the degree that poloidal fields bend, with $m \rightarrow \infty$ giving a pure vertical field. We chose $m = 0.5$ the same as Bai & Stone (2017). We also applied the same disk setup to a hydro-only run, adopting an $\alpha = 0.001$ and without the magnetic field.

2.2 Planet

The planet is held on a fixed circular orbit at $r_p = 10$ code units (c.u. hereafter) in the disk midplane. The planet-to-primary mass ratio q is set to 0.001, corresponding to the Jupiter mass around a Sun-like star, equivalent to 5.12 thermal mass. The total gravitational potential Φ considered in the simulation is $\Phi = \Phi_* + \Phi_p$, where $\Phi_* = -GM_*/r$ is

the gravitational potential of the central star, and Φ_p is the potential of the planet, given by:

$$\Phi_p = -\frac{GM_p}{\sqrt{|\mathbf{r} - \mathbf{r}_p|^2 + r_s^2}} \quad (4)$$

where M_p is the planet mass, \mathbf{r} and \mathbf{r}_p are vectors of each grid cell center and of the planet from the central star, and $r_s = 0.095$ is a smoothing length chosen to be 2.35 times the smallest cell size in the planet's vicinity. We ignore the indirect potential term that is due to the offset between the central star and center of gravity of the star-planet system, as it has a negligible impact on the perturbation structure (Miranda & Rafikov 2019). We also ignore the planet's mass increase due to accretion since it is small during the simulation. To minimize the influence of sudden planet insertion, the planet's mass is linearly increased with time, from zero at the start of the simulation to its final value at the time $t = 2.3 \tau_p$ where τ_p is the planet's orbital period.

2.3 Magnetic Diffusion

In a protoplanetary disk, we consider a weakly ionized fluid composed of ions, electrons, charged grains, and neutrals. We will only consider Ohmic dissipation and ambipolar diffusion, with the following induction equation governing the magnetic field evolution:

$$\frac{\partial \mathbf{B}}{\partial t} = \nabla \times (\mathbf{v} \times \mathbf{B}) - \frac{4\pi}{c} \nabla \times (\eta_O \mathbf{J} + \eta_A \mathbf{J}_\perp). \quad (5)$$

Here $\mathbf{J}_\perp = \mathbf{B} \times (\mathbf{J} \times \mathbf{B})/B^2$ is the current density perpendicular to the magnetic field, and η_O and η_A are the Ohmic and ambipolar diffusivities, respectively.

The magnetic diffusivities, particularly η_A , depend strongly on the abundance and size distribution of dust grains, especially small grains, which can become the main charge carriers in dense regions of protoplanetary disks (Wang et al. 2019). Ideally, they should be computed through consistent thermochemistry simultaneously with the magnetohydrodynamics. However, the computation is prohibitively expensive, which motivates us to employ the look-up table¹ from our precursor study where we adopted a 2D r - θ domain assuming axisymmetry (Hu et al. 2023). The 2D model used a planetary torque to open a gap and tracked the evolution of magnetic diffusivities in the gap center to assemble the look-up table. In the full thermo-chemical setup, the disk has a midplane density of $8 \times 10^{-12} \text{ g cm}^{-3}$ at 10 au, which corresponds to a gas surface density of 170 g cm^{-2} . 10 au is also the planet's distance to the central star, which equals 10 c.u. hereafter. There are 28 chemical species, including charged grains. Ionization sources include ray-tracing FUV and X-ray flux from the central star and diffused ionization from down-scattered X-ray, cosmic ray, and short-lived radioactive nuclei. We refer the reader to Hu et al. (2023) and references therein for a more detailed description. For the ambipolar diffusion, we obtain the Elsasser number Am from the table; for the Ohmic resistivity, we directly obtain the diffusivity η_O from the table. There's a simple monotonic trend between η_O and

¹ The table is available in both Python and C scripts at <https://github.com/astroxhu/diffusion-table>

the local density for the Ohmic resistivity. The Am look-up table is a function of the local density normalized by the initial midplane value $\rho/\rho_{\text{mid},0}$ and the vertical location normalized by the scale height z/h . There are two motivations to use $\rho/\rho_{\text{mid},0}$ instead of the absolute value. First, we'd like to keep our 3-D setup as scale-free as possible. The original 2-D run used absolute density because of the chemical network. Second, the constant $Am \sim 10^{-2}$ along the midplane is a good approximation for the full thermochemical model. The Am 's location dependence is within 2h, where the cosmic ray ionization is more attenuated from the column density. The Am vertically varies only within 2h from the midplane, where the cosmic ray ionization is significantly attenuated due to the higher column density. Above that Am only relies on $\rho/\rho_{\text{mid},0}$. There is an Am "valley" just below the disk surface, reaching $\sim 3h$. This trend resembles the power-law prescription proposed by Suriano et al. (2018) where the Am inside the disk decreases with a decreasing density as a result of balancing the recombination of the dominant ions and electrons with the cosmic ray ionization, as discussed in Hu et al. (2023).

Since the look-up table is obtained in an environment where the radiation from the central star is sufficiently shielded, it only works well for the denser part of the disk, not the disk atmosphere. Thus, we keep the diffusion profile unchanged from the initial setup for any region more than $4h$ from the midplane.

2.4 Boundary Conditions

A modified outflow condition is employed for hydrodynamic quantities for the inner radial boundary. Here, the vector quantities' r and θ components are duplicated from the last active grid cell into the ghost zones. We extrapolate the initial power-law distribution for the density ρ (i.e., Eq. 1) and the Keplerian rotation for v_ϕ into the ghost zones. When directed toward the active simulation domain, the radial components of the vector quantities are set to zero in the ghost zones. The azimuthal magnetic field component (B_ϕ) is set to zero at the inner radial boundary. At the outer radial boundary, all hydrodynamic and magnetic quantities are replicated from the active zones into the ghost zones, except when the radial velocity (v_r) is negative; in which case v_r is set to zero in the ghost zones. Reflecting boundary conditions are applied at the θ boundaries adjacent to the polar axis. A periodic boundary condition is utilized in the ϕ direction.

3 MODEL RESULTS

To give a first impression of the simulation, we show in the top right part of Figure 1 the density distribution on the meridional plane through the planet at a representative time $t = 100 \tau_p$, with the statically refined grid structure superposed. The top left panel shows a 3D view of an iso-density surface, highlighting the radial variation of the disk thickness induced by the planet and non-ideal MHD effects. The lower part of the figure shows the distribution of the vertical component of the velocity on the midplane, highlighting the substructures formed in the disk.

The surface density evolution over 115 planet's orbital periods (τ_p) is shown in Figure 2a, with the colormap illustrating the radial distribution of azimuthally averaged surface density normalized by the initial distribution $\Sigma(r)/\Sigma_0(r)$. The surface density at the gap center reaches about 1% of the initial value after $100 \tau_p$. Similar to Aoyama & Bai (2023), there's no apparent radial width asymmetry between the parts of the gap inside and outside the planet's orbit. This is also seen in the $Mj - \beta_4$ case from Wafflard-Fernandez & Lesur (2023), which has the same planet mass and relative magnetic field strength as our setup. We also find the magnetic field is significantly strengthened in the gap (see Figure 2b and also panel (d) of Figure 8 in Section 3.1). The magnetic flux concentration is relatively stable at later times, with the concentrated flux staying near the gap center, similar to the $Mt1Am3$ case in Aoyama & Bai (2023). This behavior is different from the $Mj - \beta_4$ case of Wafflard-Fernandez & Lesur (2023), where the location of magnetic flux concentration oscillated in the gap, leaving some isolated hot spot on their spacetime diagram, or their $Mj - \beta_3$ case, where the concentration diverges to the gap edges when the gap widens and becomes radially asymmetric.

We plotted the gas surface density snapshots at two representative times in Figure 3. Panel (a) shows that the gap starts to be opened at $t=50 \tau_p$, with two prominent spiral density wakes, just as in a viscous disk. Both spiral wakes leave some secondary density perturbations, and the outer one seems to be more significant. There is a slight density bump in the gap since the gap is still getting deeper. The minimum density is seen at the leading and trailing edge of the planet. The gap has not shown azimuthal asymmetry at this point. In panel (b), the gap is well formed at $t=100 \tau_p$ and in a steady phase, with a width roughly twice that of the planet's Hill sphere, highlighted with a solid circle. The density bump in the gap is gone, and only a few % of gas remains at the gap center. A slight azimuthal asymmetry exists, with some mass concentration between L5 and the planet. The density perturbations ($R \sim 17$ c.u.) from the outer spiral wake are persistent, and almost form a full 2π gap. Panel (c) of Figure 3 illustrates the velocity field on the midplane around the planet, with the arrows showing the classic horseshoe orbits and the rotating flow pattern inside the Hill sphere surrounding the dense circumplanetary disk and the colormap showing the midplane variation of the vertical velocity component.

Figure 4 shows the azimuthal average of the ambipolar diffusion Elsasser number Am and the Ohmic resistivity η_O obtained from the look-up table on a cylinder at the gap center's radius. Note the azimuthal average excludes the region within about 4 times the Hill sphere of the planet. Initially, the disk is most magnetically diffusive near the midplane (with the smallest Elsasser number), where the ionization level is low because of excessive recombination on the grain surface. The reduction of magnetic diffusion is relatively modest in the first $60\tau_p$, with a factor-of-3 increase in Am and less than 50% decrease in η_O . In contrast, by $t=100\tau_p$, the Am near the midplane has increased by nearly two orders of magnitude, yielding an almost constant vertical profile with values close to unity, which, coincidentally, is similar to the fixed Am value adopted by both Aoyama & Bai (2023) and Wafflard-Fernandez & Lesur (2023) in the

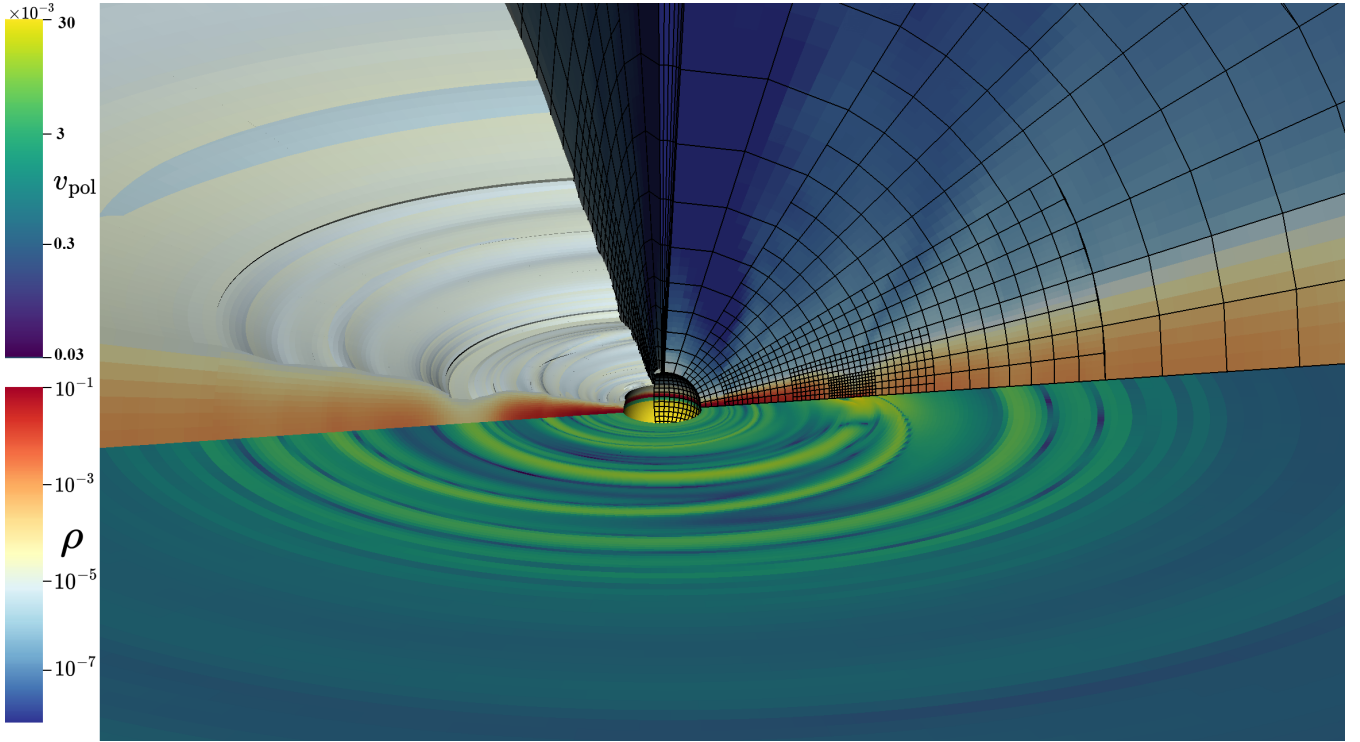


Figure 1. The simulation at the representative time $t=100 \tau_p$. The colormap in the top right part of the figure is the gas density distribution on the meridional plane passing through the planet, where the grid is the most refined (see the black grid, with each cell representing 4×4 simulation cells). Shown in the top left is a 3D view of an iso-density surface, highlighting the radial variation of the disk thickness induced by the planet and non-ideal MHD effects. The 2D colormap in the foreground (the lower half) plots the vertical velocity component on the midplane, illustrating the substructures developed in the disk.

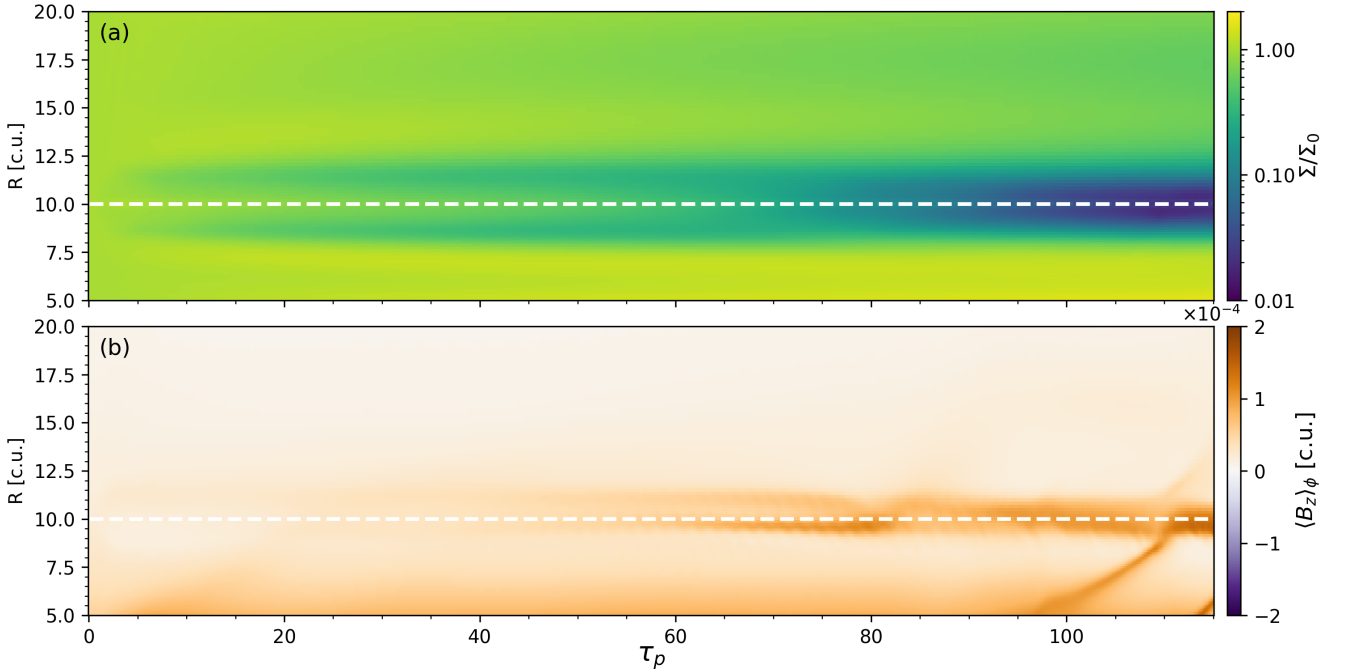


Figure 2. Space-time diagrams showing the evolution of (a) the gas surface density relative to its initial profile (Σ/Σ_0) and (b) the azimuthally averaged midplane vertical field strength (B_z). The location of the planet is marked with a white dashed line.

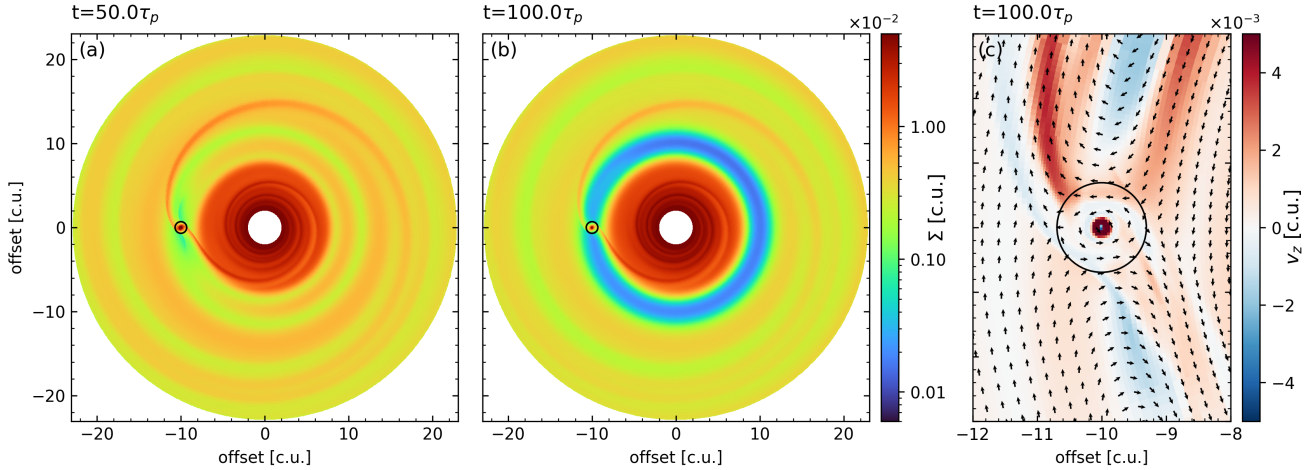


Figure 3. Snapshots at $t=50$ and $100 \tau_p$. The color maps in panels (a) and (b) are the gas surface density in code units (c.u.). The black circle highlights the location and size of the planet’s Hill sphere. Panel (c) shows a zoom-in view of the gas velocity structure, with the arrows representing the midplane velocity vectors in the planet’s rest frame. The color map is the midplane vertical velocity.

disk. The Ohmic resistivity profile retains its initial shape, with a strength reduced by an order of magnitude. We also overplotted the diffusion profiles at a radius not in the gap, where the Elsasser number and Ohmic resistivity retain their initial distributions (dashed line) at $100\tau_p$. Unlike the two previous studies, the jump in magnetic diffusivities from the rest of the disk to the gap in our setup implies some interesting gas dynamics at the gap edge (see Section 3.1). Figure 4 demonstrates that mass depletion makes the gap region better magnetically coupled compared to the initial disk midplane, which has implications on its dynamics.

We choose to perform diagnostics of the simulation in cylindrical coordinates to simplify angular momentum analysis. The azimuthally averaged $R\phi$ and $z\phi$ stresses govern the disk angular momentum transport:

$$T_{R\phi} = \frac{1}{2\pi} \int_0^{2\pi} [\rho v_R (v_\phi - \bar{v}_\phi) - B_R B_\phi] d\phi \quad (6)$$

$$T_{z\phi} = \frac{1}{2\pi} \int_0^{2\pi} [\rho v_z (v_\phi - \bar{v}_\phi) - B_z B_\phi] d\phi \quad (7)$$

In both formulas, \bar{v}_ϕ is the azimuthally averaged toroidal velocity, the first term inside the integral denotes the contribution from Reynolds stress, and the second term represents Maxwell stress. In a (quasi-)steady accretion disk, the accretion is driven by the radial gradient of $T_{R\phi}$, the difference of the $T_{z\phi}$ between the top (marked as t as integration limit, where $\theta - \pi/2 = -0.25$) and bottom disk surfaces (marked as b as integration limit, where $\theta - \pi/2 = 0.25$), and the torque from the planet $\Gamma_p = \frac{1}{2\pi} \int_b^t \int_0^{2\pi} \rho(\mathbf{r}_p \times \nabla \Phi_p) d\phi dz$, namely,

$$\begin{aligned} \frac{\dot{M}_{\text{acc}} \Omega_K}{4\pi} &\simeq \frac{1}{R} \frac{\partial}{\partial R} \left(R^2 \int_b^t T_{R\phi} dz \right) + R [T_{z\phi}]_b^t - \Gamma_p \\ &= \mathcal{R}_{R\phi} + \mathcal{M}_{R\phi} + \mathcal{R}_{z\phi} + \mathcal{M}_{z\phi} - \Gamma_p \end{aligned} \quad (8)$$

Here \dot{M}_{acc} is the accretion rate within the disk, and v_K is Keplerian orbital velocity. We used \simeq as we approximate the disk’s v_ϕ by the Keplerian speed, since the azimuthally averaged v_ϕ is within 4% of v_K at the midplane. Then we have $\dot{M}_{\text{acc}} \partial(rv_\phi)/\partial r \simeq \dot{M}_{\text{acc}} \partial(rv_K)/\partial r = \dot{M}_{\text{acc}} v_K/2$ for the radial transport of angular momentum under a constant mass

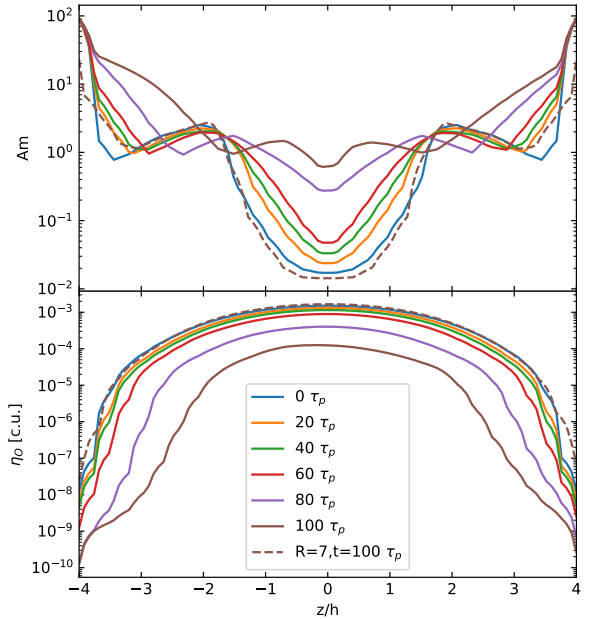


Figure 4. Evolution of the vertical profiles of the magnetic diffusivities at the gap center, up to $100\tau_p$. The ambipolar diffusion Elsasser number Am is in the upper panel, and the Ohmic resistivity η_O is in the lower. Plotted are the vertical distributions of the azimuthally averaged diffusivities, excluding the region near the planet. The same color code is used in both panels to indicate the time of the snapshot. The dashed lines in both panels show the diffusion profiles of a region ($R=7$ in code unit, c.u. hereafter) that is not in the gap.

accretion rate. It is worth noting that this approximation introduces a deviation of up to 50% at the gap edge due to the alteration of the rotation curve caused by the planet. However, this does not affect our analysis, as we will only compare the terms on the right-hand side of Equation 8. Following Wafflard-Fernandez & Lesur (2023), we divided the stress terms on the right-hand side of Eq. 8 into its Reynolds

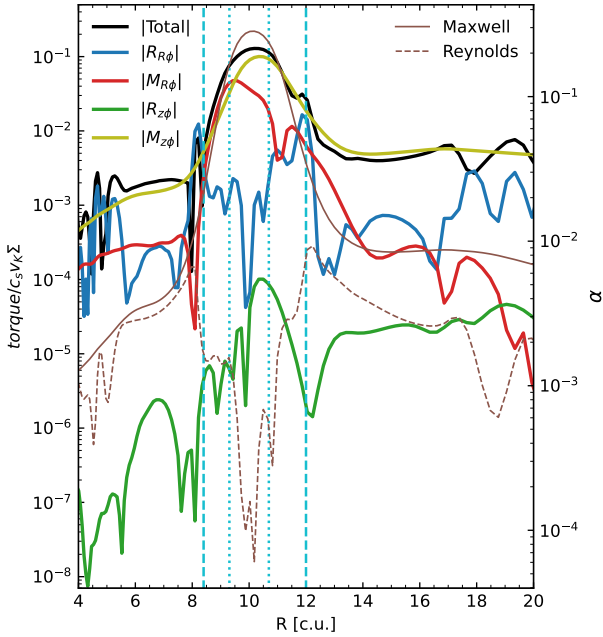


Figure 5. Radial profile of the absolute values of the four torques $\mathcal{R}_{R\phi}$ (blue), $\mathcal{M}_{R\phi}$ (red), $\mathcal{R}_{z\phi}$ (green), $\mathcal{M}_{z\phi}$ (yellow), and the total torque (black). All torques are normalized by $c_s v_K \Sigma$ and azimuthally-averaged and temporally-averaged from $t=90\tau_p$ to $100\tau_p$. Scaled by the right y-axis, the thin brown solid and the thin brown dashed lines are the Maxwell α and the Reynolds α , respectively. The cyan vertical lines mark the area of the corotation region (dashed) and the planet’s Hill sphere (dotted).

and Maxwell component, written in the second row. The four terms that can contribute to the total planet-free torque are the radial Reynolds ($\mathcal{R}_{R\phi}$) and Maxwell ($\mathcal{M}_{R\phi}$) torques and the $z\phi$ Reynolds ($\mathcal{R}_{z\phi}$) and Maxwell ($\mathcal{M}_{z\phi}$) torques. Figure 5 shows the contribution of the absolute value of these four torques to the disk accretion as a function of the distance to the star. All torques are scaled to $c_s v_K \Sigma$ to get the dimensionless v parameter defined in Lesur (2021). The Maxwell wind torque ($\mathcal{M}_{z\phi}$, yellow line) is the dominant term in the whole radial range, which means the angular momentum transport is mainly through magnetic wind loss through the disk surface. The next two contributions are both torques due to radial stresses, the Maxwell ($\mathcal{M}_{R\phi}$, red line) and Reynolds ($\mathcal{R}_{R\phi}$, blue line) components, which are comparable outside the gap. With the gap edges marked by two vertical dashed lines, we find that both Maxwell torques are enhanced by about an order of magnitude inside the gap, while the radial Reynolds torque is suppressed relative to its Maxwell counterpart. The magnetic flux concentration and gas depletion in the gap are both contributing to this difference. The Reynolds wind torque ($\mathcal{R}_{z\phi}$, green line) contributes little to the total accretion.

The relative strength of $R\phi$ stress can be characterized by the equivalent Shakura-Sunyaev α parameter, defined as the ratio of the vertically integrated $R\phi$ stress to the thermal

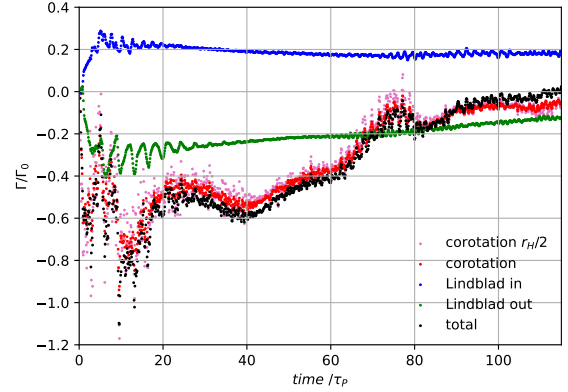


Figure 6. Evolution of the migrational torques acting on the planet in the fiducial setup, normalized by Γ_0 . Plotted are the corotational torque (red dots), Lindblad torques from the disk gas outside the outer edge (green) and inside the inner edge (blue) of the corotation region, and the total torque (black). The pink dots represent the corotational torque calculated with half tapering radius.

pressure in the disk ($\pm 3.5h$):

$$\alpha_{Max} = \left| \int_b^t \int_0^{2\pi} B_R B_\phi d\phi dz \right| / \left| \int_b^t \int_0^{2\pi} P_{gas} d\phi dz \right| \quad (9)$$

$$\alpha_{Rey} = \left| \int_b^t \int_0^{2\pi} \rho v_R (v_\phi - \bar{v}_\phi) d\phi dz \right| / \left| \int_b^t \int_0^{2\pi} P_{gas} d\phi dz \right| \quad (10)$$

The Maxwell and Reynolds α 's are plotted in Figure 5, with scaling given on the right y-axis. The magnitude of α_{Rey} is just a fraction of α_{Max} , and they show a similar trend inside the gap as $\mathcal{R}_{R\phi}$ and $\mathcal{M}_{R\phi}$. The planet creates two large-scale structures: the gap and two spiral-density waves. Because $\mathcal{R}_{R\phi}$ relies on the radial gradient of the $R\phi$ stress, those two structures can boost the contribution from the Reynolds component. The sharp drop of α_{Rey} at the gap edges results in the highest value of $\mathcal{R}_{R\phi}$, almost dominating the total torque at these locations.

The Type II migrational torque is divided into the corotational and Lindblad torque. We first identify the corotational region by checking the velocity vectors in the mid-plane, and the region is set by $8.4 < R < 11.8$, roughly five times the planet’s Hill radii. The Lindblad torque Γ_L is simply the sum of the torque of all cells outside this cylindrical zone, and we calculate the torque from the inner and outer disk separately. For the torque from the corotational region Γ_C , in addition to the same softening length used in Eq. 4, we minimize the effect of the gas inside the Hill sphere by multiplying a taper function $f_H = 1 - e^{-|r - r_p|^2 / r_t^2}$, where r_t is the tapering radius. We compare two choices of r_t : the fiducial $r_t = r_H$ used in FARGO (Masset 2000) and $0.5r_H$. While the latter exhibits higher fluctuations, the overall behavior of both tracks remains consistent and overlaps. Γ_C dominates the total torque when $t < 75\tau_p$, as shown in Figure 6. We normalized the torque by the characteristic scaling (e.g., Paardekooper et al. 2010) $\Gamma_0 = q^2 (h/r)^{-2} R_p^4 \Omega_p^2 \Sigma_p$. Both Γ_C and Γ_L are negative torques in this early phase. After $100\tau_p$, the corotational torque drops to near zero, and the Lindblad torque is reversed to be slightly positive, and so is the combined total torque.

An intriguing effect of the MHD wind is that it can sup-

press the planet accretion by removing gas in the mass reservoir. Though we don't have a mass sink for proper long-term planetary accretion study, we can monitor the gas concentration near the planet. We do so by computing the masses enclosed within three spheres centered on the planet, with radii of $1 R_H$, $0.3 R_H$, and $0.1 R_H$. We take mass within $0.3 R_H$ as a proxy for the circumplanetary disk (CPD) mass (based on an inspection for the surface density distribution near the planet; see, e.g., Figure 3b), shown as orange lines in Panel (a) of Figure 7. The same mass measurement is performed for the hydro case with viscous $\alpha = 0.001$, plotted as dashed lines of the same color. We use black lines in Panel (b) to represent the gap depth Σ/Σ_0 at $R = R_p$. We did not exclude the gas in the planet's vicinity when measuring Σ . This may cause some spikes in the time evolution track, but not the general trend. The mass time evolution follows a smooth curve in the viscous disk. In the MHD case, a significant increase in the rate of mass loss within the Hill sphere is observed compared to the hydro case after $\approx 75 \tau_p$. We also observed the drop of plasma β (vertically averaged from -h to +h in the midplane) at the same epoch, plotted as the solid red line in Panel (b), with the scaling shown on the right y-axis. The gap depth time evolution has a similar trend, i.e., the MHD case closely follows the hydro case in the first ≈ 60 orbits. The MHD gap opening process in this early stage behaves similarly to a pure hydro process without a significant magnetic field concentration. After the magnetically driven accretion starts in earnest, it quickly depletes the gap region with a high radial velocity. The result is a less massive CPD compared to the hydro case. We cannot confirm if this is due to direct wind loss from the CPD itself. Nevertheless, the strong magnetization and better field-matter coupling in the gap region and the associated fast accretion have a negative impact on the mass reservoir for the planet growth.

3.1 Gas Dynamics of the Gap

To better illustrate the global structure of the gap, we azimuthally averaged the gas properties excluding the region close to the planet (15° sector on each side of the planet). Figure 8 (a) and (b) show that the distributions of the gas density and ambipolar Elsasser number Am are broadly mirror-symmetric with respect to the disk midplane. It is not the case for the poloidal magnetic and velocity fields, however. The Am profile roughly follows the gas density. While Am generally anti-correlates with ρ , there is an Am "valley" just below the disk surface (see the greenish layer below the reddish surface layer in Figure 8b), which resembles the power-law prescription proposed by Suriano et al. (2018) where the Am inside the disk decreases with a decreasing density as a result of balancing the recombination of the dominant ions and electrons from cosmic ray ionization. In panel (c), there's a region of high poloidal velocity ($> 0.5c_s$) just below the midplane. Its spatial distribution is associated with the kinks on poloidal magnetic field lines in panel (b). This is also reflected in panels (d) and (f), where the fast accretion happens in the layer where B_ϕ changes sign and the plasma $\beta = 2P_{gas}/B^2$ has a local maximum (because of a vanishing B_ϕ). This layer lies significantly below the midplane, indicating that the accretion is not mirror-symmetric with respect to the midplane (see panel [e]), un-

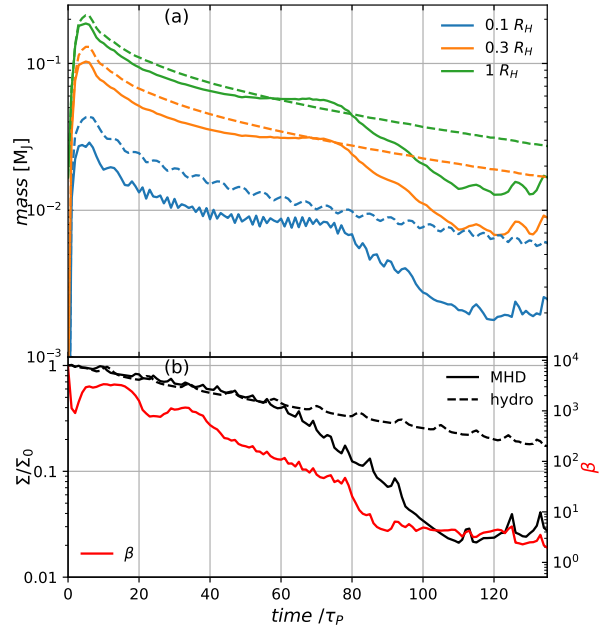


Figure 7. Panel (a): Time evolution of gas mass enclosed within spheres of 1 , 0.3 , and $0.1 R_H$ (Hill radius) centered on the planet. The solid lines represent the fiducial MHD case, and the dotted lines are from the hydro case with viscous $\alpha = 0.001$. Panel (b): The black lines are the relative gap depths for the MHD (solid) and hydro (dashed) cases, and the red line is the vertically averaged plasma β at the gap center in the MHD case, with the scaling shown on the right y-axis.

like the density distribution. Note again that the gap is significantly magnetized, with a plasma- β typically between 1 and 10 , much less than the initial midplane value of 10^4 .

In Figure 9, we present the intricate meridional flow structure within the gap, visualized through line integral convolution (LIC). Beyond the noticeable outflows at the disk's upper and lower surfaces, a particularly prominent feature is the persistent one-sided accretion stream. This stream originates from the lower surface beyond the outer gap edge (> 14 c.u.), traverses almost uninterrupted across the bottom half of the gap, and eventually converges with the accretion flow within the inner gap edge (< 6 c.u.). Notably, several elongated vortices form between the accretion layer and the disk wind emanating from the lower surface. Within the gap, near the disk's midplane, a significant circulation pattern is observed above the accretion layer. This pattern denotes a transition from accretion below to outflow above. Additionally, the wind is launched from a lower surface in the gap (see the poloidal velocity in Figure 8c), especially for the upper side. This allows the disk wind to directly impinge on the ridge of the outer gap edge, which could intensify decretion at this location in conjunction with planetary torque. The outgoing flow at the outer edge is vertically extended across the disk midplane, creating another elongated vortex between itself and the accretion stream near the bottom disk surface.

To determine if the accretion layer spans the entire azimuth of the gap and to directly compare the accretion structure before and after the gap's full formation, we analyzed the radial velocity distribution on a cylindrical surface paral-

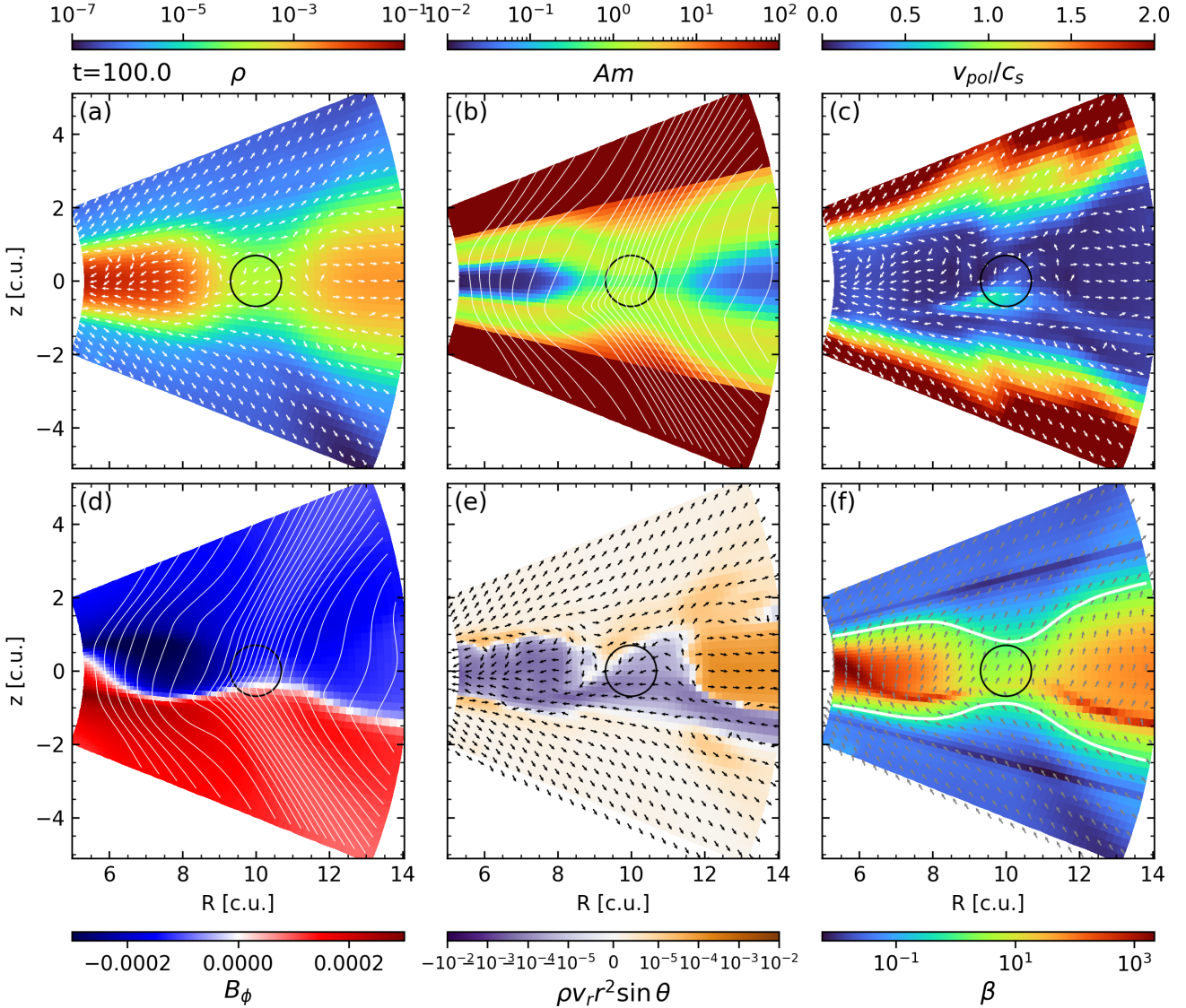


Figure 8. Azimuthally averaged gas properties at the gap excluding the planet. Panel (a): gas density (in code units) with white arrows representing velocity vectors in the poloidal plane; (b): ambipolar Elsasser number and poloidal magnetic fields (solid white lines); (c): poloidal velocity divided by the local sound speed with white arrows representing velocity vectors in the poloidal plane. Panel (d): Azimuthal magnetic field B_ϕ and poloidal magnetic fields (solid white lines); (e): effective radial mass flux per unit area and poloidal velocity vectors (black arrows); (f): plasma β and magnetic field vectors in grey arrows, with the white contour marking $\beta = 1$. The solid black circle in each panel shows the planet's Hill sphere. See the supplementary online material for an animated version of this figure.

l to the disk's rotation axis at $R=10$. For comparison, Figure 10(a) presents the time-averaged data from 40 to 50 τ_p . Beyond the planet's immediate vicinity, accretion concentrates at $\pm 2h$, just below the disk surfaces, aligning with the 2D findings of Wang et al. (2019). This accretion layer spatially correlates with the locations of significant field lines bending, which in turn are linked to significant wind stress, $M_{z\phi}$. On the midplane (where $z = 0$), the azimuthal distribution of v_R changes sign at the planet's position, with a lower absolute value at locations away from the planet than in the accretion layer. Gas flows inward on the leading side ($\phi > \pi$) and outward on the trailing side, characteristic of the horseshoe region in a viscous disk. Only the gas at the

wind base (approximately $\pm 4h$) and adjacent to the planet reaches a radial velocity exceeding $0.5 c_s$.

After the gap fully opens, the kinks in the magnetic field lines that are originally near both disk surfaces ($\pm 2h$) merge around $-h$ (Figure 10b). The azimuthal component of the Lorentz force $F_{L,\phi} \propto (\mathbf{j} \times \mathbf{B})_\phi \approx j_r B_\theta$ (since $B_\theta \gg B_r$), where $j_r \propto (\nabla \times \mathbf{B})_r = \frac{1}{r \sin \theta} \left(\frac{\partial}{\partial \theta} (B_\phi \sin \theta) - \frac{\partial B_\theta}{\partial \phi} \right)$. Since B_θ varies slowly in the disk along the θ direction, the strength of j_r resembles the magnetic torque². The grey contours in

² We use spherical coordinate here instead of cylindrical coordinates for two reasons: first, the spatial derivation is more accurate in spherical form as it follows the grid structure; second,

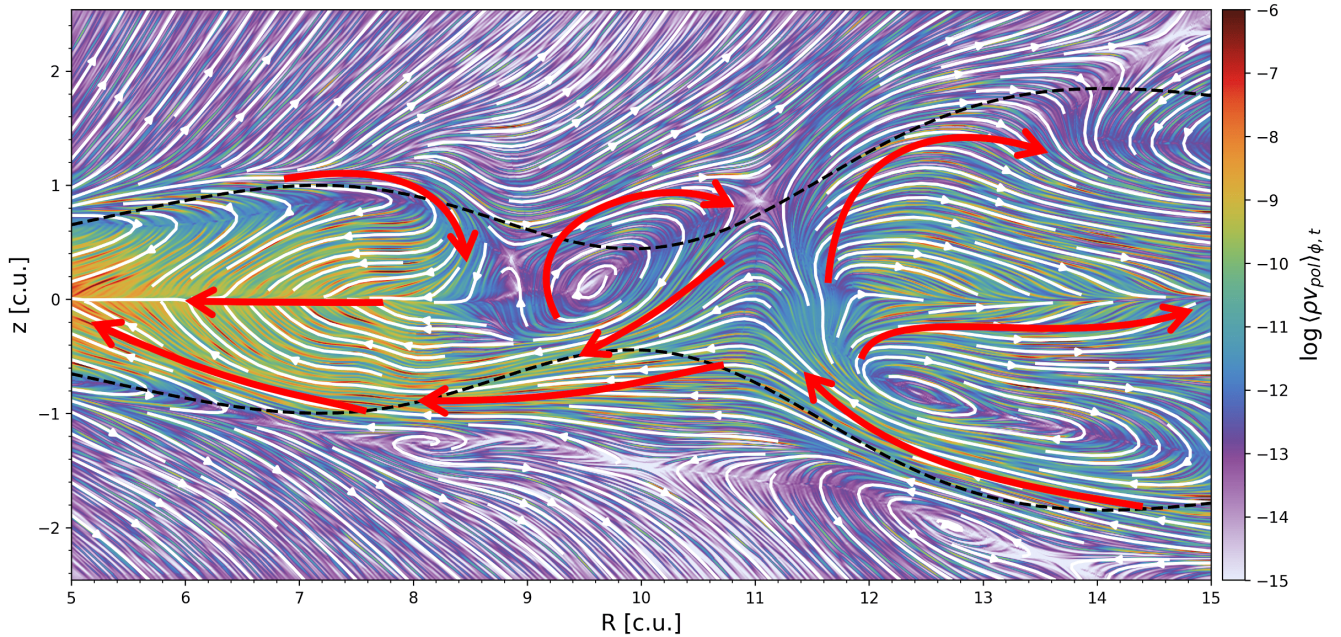


Figure 9. Meridional flows in and around the gap, averaged in azimuth (excluding the planet) and from $t=90\tau_p$ to $t=100\tau_p$. The flow structure is highlighted with LIC and white streamlines. The black solid lines are the “emission surface” with $z_0 = 0.2$ to be used in Section 3.2. The red arrows assemble a schematic view of the overall flow structure.

Figure 10(b) marks $j_r = 5 \times 10^{-4}$ in code units, roughly 1/3 of the maximum value. Between the gray contours, the region with the highest j_r is closely associated with the rapid accretion layer. After $t=80 \tau_p$, the break from the mirror symmetry across the planet in the azimuthal distribution of the radial mass accretion becomes prevalent, significantly reducing the horseshoe region’s size on the planet’s trailing side. The streamlines in Figure 11, drawn based on the velocity of cells with the highest j_r , further confirm that the Lorentz force directly enables the fast accretion layer. A minor over-density is observed between the planet and the trailing Lagrangian point L5, likely due to material accumulation by the vortex from the reduced horseshoe orbit. The pronounced asymmetry in streamlines is also observed in case $Mj - \beta 3$ from Wafflard-Fernandez & Lesur (2023), where the horseshoe region narrows to a zone with limited azimuthal extent, potentially leading to a similar dust distribution. Wu et al. (2023) proposes that these asymmetric dust clumps could serve as observational indicators of wind-driven accretion.

3.2 Observational Implications

In this section, we extract the gas kinematics in a way similar to that used for recent ALMA line observations (e.g. Teague et al. 2021; Izquierdo et al. 2021). Unlike Hu et al. (2023), who marked the emission surface with a constant column density from the top of the simulation domain, we choose to

the strongest current deviates more than one scale height from the midplane, which makes the spherical r better represents the direction of accretion than the cylindrical R .

model the shape of the emission surface using the analytic function suggested in the molecular line data analysis tool eddy (Teague 2019):

$$z(R) = z_0[1 - g(R)](R - R_c)^\Phi \exp\left[\left(\frac{R - R_t}{R_t}\right)^{q_t}\right] \quad (11)$$

We choose $z_0 = \pm 0.1, 0.2, 0.3$, $R_c = 1$ c.u., $\Phi = 1$, $q_t = 2$, and $R_t = 9$ c.u. for our model. Within the tapering radius R_t , $z_0 = \pm 0.1, 0.2, 0.3$ each translates to 1.7, 3.5, and 5 scale heights above/below the midplane. The vertical modulation $g(R) = d_0 \exp[-(R - R_p)^2/(2w_h^2)]$ is a Gaussian function that adds the gap shape to the smooth surface, where $d_0 = 0.75$ is the maximum relative gap depth in z/R . $R_p = 10$ c.u. is the planet’s orbital radius, and $w_h = 1.6$ is the half-width. The drop in emission surface at the gap is found in disks like AS209 (Galloway-Sprietsma et al. 2023), HD163296, and MWC480, after carefully masking the channel emission (Paneque-Carreño et al. 2023; Izquierdo et al. 2023). We choose the median value $z_0 = \pm 0.2$, i.e., $z \sim \pm 3.5h$ where $R < R_t$ as the simulated emission surface (see the dashed lines in Figure 9). The velocities v_r , v_θ , and v_ϕ are averaged over one scale height, weighted by the gas density. We project the velocity vectors to the line of sight (LOS) at an inclination $i = 45$ deg, with the planet lying on the vertical line on the near side of the inclined disk. Assuming one code length unit equals one au, we get the 2D LOS velocity distribution in m/s in Figure 12, with meshes highlighting the shape of the “emission surface.” Note that this parametric surface does not accurately represent the real-life emission surface of any specific molecule. Instead, it serves as a demonstration of the velocity distribution on a layer distorted by a deep gap. Factors such as chemical abundance, gas temperature, and velocity gradient all contribute

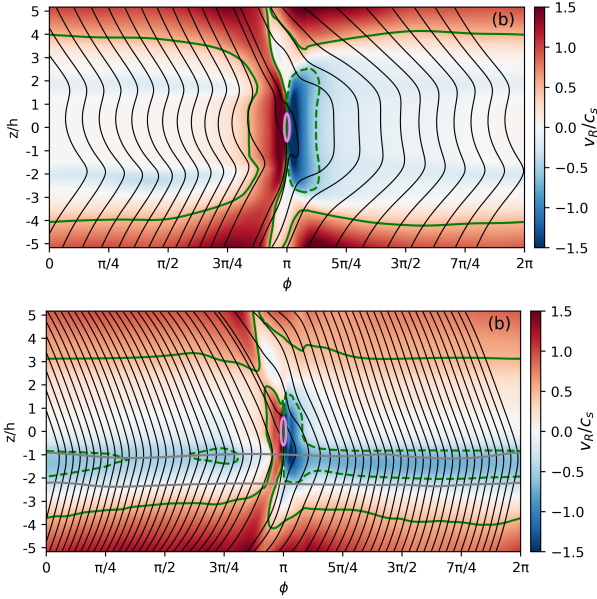


Figure 10. Gas radial velocity scaled to the midplane sound speed of a $z - \phi$ slice at the planet’s orbit. Panel (a) is a time average from 40 to 50 τ_p , and panel (b) is from 90 to 100 τ_p . The magnetic field in the $z - \phi$ plane is plotted as black solid lines, and both panels used the same magnetic flux spacing between two adjacent lines, showing a stronger field at the later time frame. The green contours mark the location where $v_R = \pm 0.5 c_s$, with dashed lines representing negative values. The violet contour at the center indicates the planet’s Hill sphere, which mainly highlights the location of the planet. It is not spherical because the height and the azimuthal angle axes are not plotted to the same scale. The area between the two roughly horizontal lines in (b) has the highest radial current density j_r .

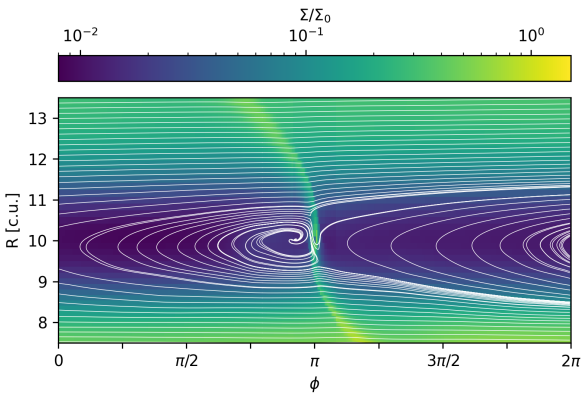


Figure 11. Streamlines around the gap at $t=100\tau_p$, plotted with the gas velocity at the layer with maximum j_r . The background colormap is the gas surface density variation Σ/Σ_0 .

to determining the shape and location of the emission surface. While the MHD disk wind could significantly alter the gas column density, its impact on the gap emission surface is expected to be less pronounced due to the substantial difference in the line-of-sight velocities between a rotating disk and a radial outflow-dominated wind (i.e., the wind does not contribute much to the optical depth and hence the location of the $\tau = 1$ emission surface at the disk’s line-of-sight veloc-

ities). Note this follows the same scaling from the look-up table of magnetic diffusivities, in which the planet is also placed at 10 au. In Figure 10, the v_R sign transition near the planet can extend up to two scale heights. It shows up clearly in the kinematics of the emission surface near the planet as a sharp transition from redshift on the leading side (to the right) of the planet to blueshift on the trailing side. Moving away from the planet, the main source of non-axisymmetric features comes from the spiral density waves. They generate notable variations in the LOS velocity map.

We notice a quasi-axisymmetric ring of redshifted gas near the gap center, which is not explainable by radial motion (accretion). To understand this feature better, we find the best fit of the axisymmetric value of v_ϕ , v_R , and v_z for the emission layer at each radius. The results are plotted in Figure 13. We also performed the same analysis on the other side of the inclined disk ($i = -45$ deg), with the results plotted as dashed lines. The gas surface density profile at the same snapshot is in the top panel for reference. Outside the gap region, there’s a shallow gap between 16 and 20 au and another shallow gap with an adjacent density bump at 4-6 au; they appear to be a consequence of the fast accretion caused by the concentrated poloidal magnetic field in the planet-opened gap, which removes mass from outside the gap to the inside of it. In contrast, the secondary inner gap in Aoyama & Bai (2023) is much deeper with a strong magnetic flux concentration. The azimuthal velocity profiles are almost identical on both sides of the disk at all three z_0 locations, except the $z_0 = 0.3$ where anywhere within 5 au would be dominated by the disk wind. For $z_0 = 0.3$, a larger deviation from the other two z_0 locations is also expected in the other two velocity components. Nevertheless, the azimuthal velocity kink is still a solid method to uncover a planetary perturbed in an MHD wind-launching disk. The radial velocity is about 50 m/s between 12 and 20 au for all cases but shows significant fluctuations in the inner disk. A feature of surface accretion driven by MHD wind is the narrow transition layer of v_R near the disk surface. Within one scale height, v_R could change its sign entirely (Figure 10a). But this could not explain the large v_R deviation in the gap for $t=100 \tau_p$. Take the middle case $z_0 = 2$ as an example, from Figure 9, we can see that the fast accretion layer completely encapsulates the bottom emission surface, while the top surface probes the large vortex just below the wind base. The same break of top-bottom symmetry is also shown in the vertical velocity. The bottom emission surface has a relatively fast flow moving away from the midplane at the planet-opened gap (see the dashed lines in Figure 13), which shows a remarkable resemblance to the flow pattern inferred from observations of the HD163296 and AS209 disks. In our case, it is caused by the accretion layer being displaced from the midplane by a large vortex, which also makes the v_z in the top emission layer jump between positive and negative values across the gap. The negative v_z near the planet’s orbit corresponds to the part of the meridional vortex that moves towards the midplane, which gives rise to the quasi-axisymmetric redshifted ring near the gap center noted earlier in the LOS velocity map (see Figure 12).

To comprehensively demonstrate the spatial distribution differences among the three velocity components, we show in Figure 14 their two-dimensional R-z color maps at $t = 100 \tau_p$, using azimuthal averaging similar to Figure 8.

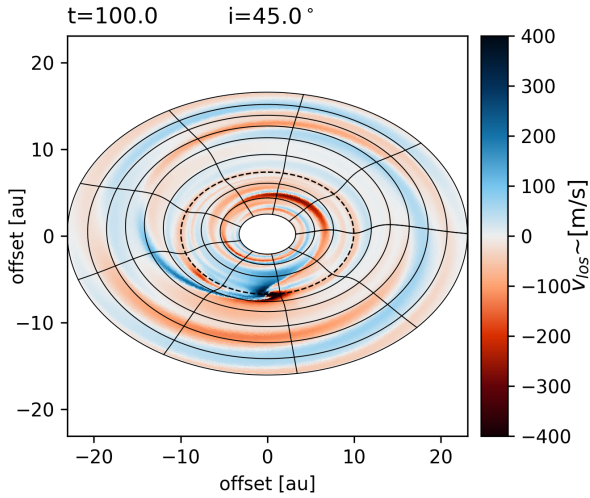


Figure 12. Line-of-sight gas kinematics extracted at the parametric emission surface, with an inclination of 45 degrees, after subtracting mean azimuthal velocity. The dashed circle marks the gap center. Note this is not the residual velocity after subtracting the three axisymmetric velocity components.

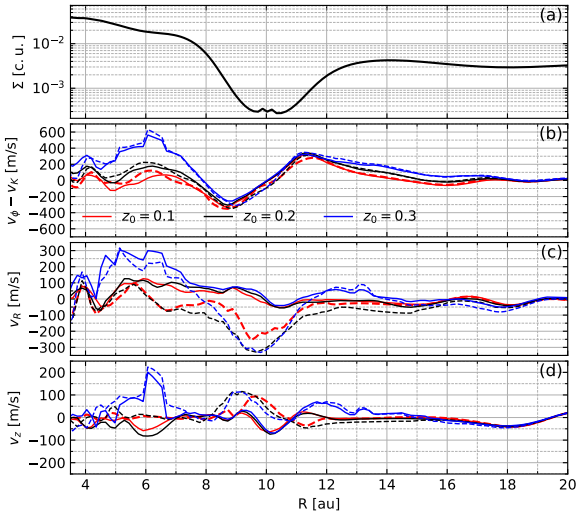


Figure 13. 1D (axisymmetric) velocity profile for three parametric emission layers: $z_0 = 0.1$ (red), $z_0 = 0.2$ (black), and $z_0 = 0.3$ (blue) at $t=100\tau_p$. The top panel (a) is the gas surface density for reference, and panels (b), (c), and (d) are ϕ velocity's deviation from Keplerian, radial velocity v_R , and vertical velocity with respect to the midplane v_z . The solid lines are from the top surface ($i=45$ deg), and the dashed lines are from the bottom surface ($i=-45$ deg). Note $v_z > 0$ refers to velocity vectors pointing away from the midplane in all cases.

As shown in Figure 13b, v_ϕ maintains mirror symmetry at different heights. The widespread sub-Keplerian region between 14-20 au is likely caused by the overpressure at the outer gap edge, resulting in a greater deviation from Keplerian motion than a disk with a smooth density profile. The distribution of v_R shows a particularly clear break in mirror symmetry across a broad region from radii 5-20 au, where the main accretion flow is near the bottom disk sur-

face, only partially extending to the upper disk surface in the gap due to a vortex. Near the midplane, both the negative v_R region inside the planet's orbit and the positive v_R region outside the orbit extend significantly in radius. The distribution of v_z also directly reveals the impact of the asymmetric accretion layer. The distribution of v_z is also asymmetric relative to the midplane, as indicated by the gap's large red triangle-shaped region to the planet's right side, and blue region across the Hill sphere. It results from the combined effects of the accretion layer and the vortex. The v_z distribution shows the general trend of gas movement in the accretion layer at the bottom surface: it first approaches the midplane from the outer gap edge (positive v_z). Then it moves back towards the surface. It is consistent with the streamlines shown in Figure 9.

We generated the $^{12}\text{CO } J=2-1$ emission map of the wind-driven accretion disk using RADMC-3D (Dullemond et al. 2012) assuming a disk inclination angle of 45° . We only included the disk region with $r < 23$ au where the midplane is mesh-refined by at least 2 levels. The temperature structure is the same as used in the MHD simulation. We annotated six features in panel (d) of Figure 15: (1) the bright spot is the disk wind that is denser than its surroundings, probably from the inner spiral density wake, and there are similar bright spots in panel (a), elevated from both top and bottom disk surfaces; (2) disk wind from the bottom disk surface has a low LOS velocity because the v_r has a positive contribution to v_{LOS} while the super Keplerian v_ϕ (counter-clockwise rotation) is negative on the LOS; (3) the velocity kink caused by the gap opening planet at the top emission surface; (4) the tiny bulge is from the circumplanetary disk; (5) and (6) are disk winds from bottom and top disk surface, and both of them have a redshifted v_ϕ and a blueshifted v_r partially canceling out each other along the LOS. The velocity kinks on the disk surface exhibit structures similar to those in hydrodynamic simulations (Izquierdo et al. 2021), aligning with the v_ϕ profile seen in Figure 13b. The planetary torque predominantly shapes the morphology of v_ϕ around the gap. Kinks also appear in the outer regions, originating from a shallow gap at 18 AU (see Figure 13a). When assuming an ISM level ($f_{\text{CO}} = 10^{-4}$) CO abundance, the disk wind extends noticeably beyond the upper and lower surfaces of the disk. However, an abundance one order of magnitude lower shows wind primarily at the disk's outer part. The wind becomes nearly invisible if the CO abundance is two orders of magnitude lower.

The current ALMA molecular line disk observations typically do not show obvious wind signatures. There are several possible reasons for the non-detection. First, our model has a relatively strong wind driven by a disk with a high accretion rate of $\sim 10^{-6} m_\odot \text{ yr}^{-1}$, which is higher than most of the relatively evolved disks with high resolution and sensitivity line observations (e.g., AS209 Zhang et al. 2021). Second, the CO abundance in disks (and the winds from them) might be one to two orders of magnitude lower than ISM values (e.g., Zhang et al. 2021), which may make it harder to detect the wind in CO; more optically thick lines, such as those from neutral carbon may be required to detect the wind. 3) The current molecular line observations typically probe disk regions larger than shown in Figure 15, where the wind could be weaker. For example, Fang et al. (2023) suggested that the MHD wind from the inner disk

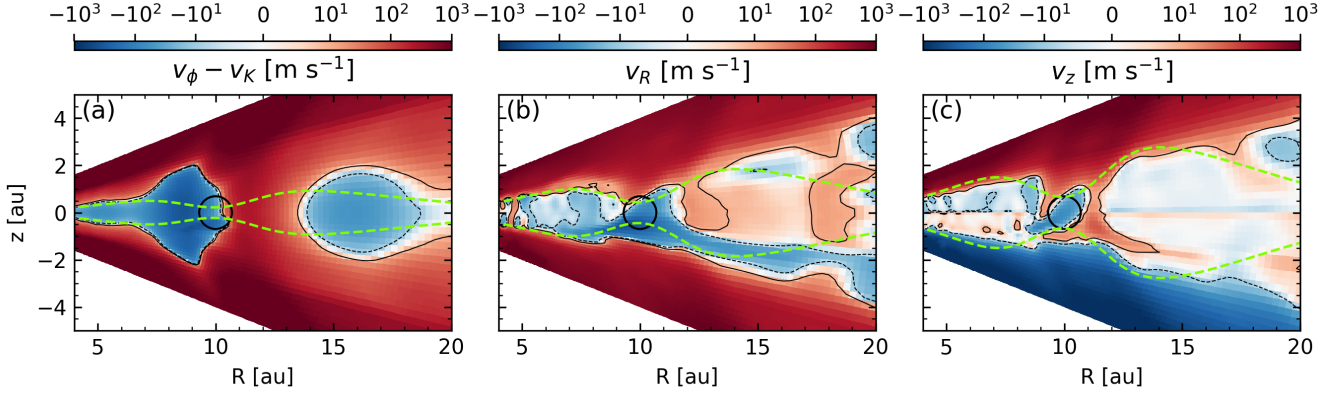


Figure 14. Azimuthally averaged map of three velocity components: (a) $v_\phi - v_K$, (b) v_R , and (c) v_z . All panels use the same “SymLog” scale with the linear threshold set to $\pm 10 \text{ m s}^{-1}$, and the solid and dashed contours are values of 10 m s^{-1} and -10 m s^{-1} , respectively. From left to right, the dashed green lines in the three panels are “emission surfaces” with $z_0 = 0.1, 0.2,$ and 0.3 , respectively.

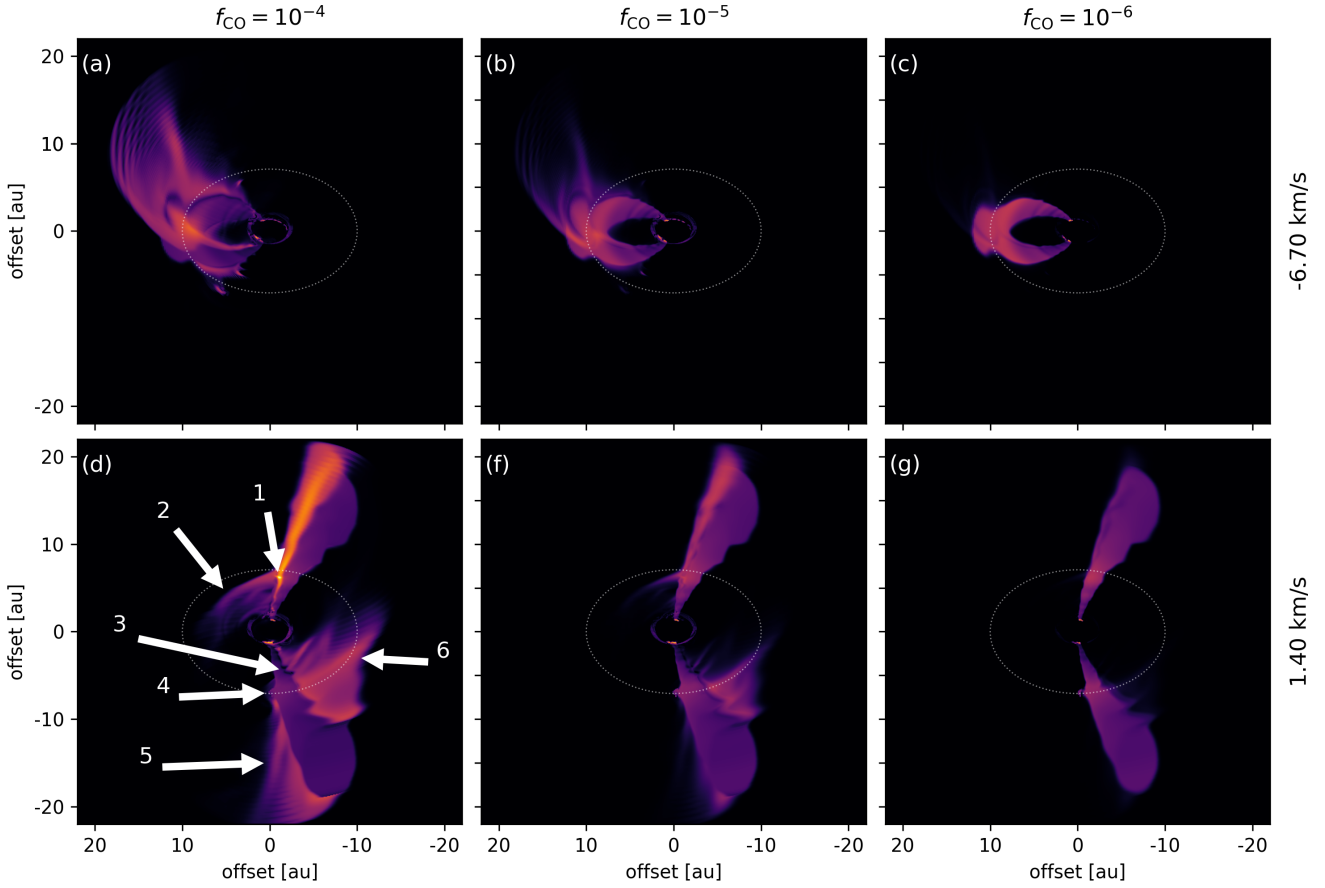


Figure 15. Synthetic line emission maps of $^{12}\text{CO } J = 2 - 1$ at two different velocity channels. The top row has a velocity of -6.7 km/s , and the bottom row is 1.4 km/s . From left to right, each column is assigned with a different CO abundance, 10^{-4} (ISM value), 10^{-5} , and 10^{-6} . The thin dotted ellipse in each panel indicates the planet’s orbit. We highlighted six features in panel (d).

can block high-energy radiation from the central star, thus inhibiting the generation of photoevaporation wind in the outer disk. Disk accretion may also concentrate the poloidal magnetic flux in the inner disk, leaving the outer disk too weakly magnetized to launch a significant wind.

3.3 Gas dynamics around the planet

In Figure 16 we plotted the gaseous and magnetic properties near the planet at the snapshot at $t=100\tau_p$. To focus on the area that's most perturbed by the planet, all panels are azimuthally averaged within 4 cells on each side of the planet. In panel (a), the dense circumplanetary disk (CPD hereafter) extends 16 cells in diameter, which is about half the size of the Hill sphere. The small size of the CPD means its kinematics signature is limited to a tiny spatial scale that makes direct observations extremely challenging. The signature of CPD is seen between ± 1.4 km/s channels in our synthetic observations with three different CO abundances (Figure 15), which reflects its large velocity dispersion in the tiny Keplerian disk. But the CPD's little "bulge" in the channel map could be easily lost after beam convolution with background noise, especially when it is close to the PPD's bright Keplerian pattern. The CPD candidate in AS209 appeared as a point source in the ^{13}CO map but not the more abundant ^{12}CO , and only in a very narrow velocity (channel) range (Bae et al. 2022). The area that produces large LOS velocity is only a small portion of the CPD, further limiting the kinematic confirmation of a Keplerian CPD through observations. In summary, molecules with less abundances may be preferred for CPD detection as they are less likely to be "overshadowed" by the emission from the PPD. On the other hand, the less abundant molecules like C^{18}O , HCN, and C_2H are usually detected with narrower spatial distributions that do not necessarily cover the CPD location (Galloway-Sprietsma et al. 2023), and/or suffer from a low signal-to-noise ratio (Law et al. 2021). Improvement in both spatial and spectrum resolution could better isolate the CPD signature, and a longer integration time is needed for future observations of CPD candidates. Inside the Hill sphere, gas accretes onto the CPD from both the south and north hemispheres and leaves the CPD through its equatorial plane. The accretion flow collides with the incoming gas from both sides of the gap, forming two lobes that isolate the CPD from the gap edges. Moving along the two poles away from the CPD, the infall towards the plane eventually transitions to an outflow. Notably, there is a puffed-up layer starting from $R=9$ c.u. separated from the inner gap edge, resulting from the enhanced density of the inner spiral density wake. This structure is truncated by the accretion flow directly above the planet when it approaches the planet's orbit. The magnetic field lines have two major features: strong concentration on the CPD and significant asymmetry with respect to the midplane. Because of the CPD's high density, the strong diffusion effectively decouples the magnetic field lines from the accretion and rotation motions inside it. However, the look-up table may overestimate the degree of decoupling (See Section 4 for a further discussion). The poloidal velocity color map saturates near the planet's polar regions in panel (c), as our local isothermal assumption supports a runaway accretion of the massive planet. Other

sonic regions include the edge of two spiral-density waves and the lower wind base in the gap.

4 DISCUSSION AND CONCLUSION

Our high-resolution 3D simulations reveal that magnetic fields significantly alter the development and morphology of the gap created by a protoplanet. Specifically, we observe that the embedded planet can lead to a concentration of the poloidal magnetic flux around its orbit, thereby enhancing angular momentum removal in the gap region. This process results in deeper and more pronounced gap formation, akin to those observed in inviscid disk models (e.g., gap depth versus time in Figure 7b), and is characterized by a fast, trans-sonic accretion layer that is asymmetrically distributed with respect to the disk midplane. Notably, the accretion layer makes both updraft and collapsing flow possible in the gap. While a disk wind may not directly limit the growth of the planet, wind-driven accretion can indeed more rapidly deplete the mass reservoir feeding the planet. This suggests that protoplanetary disks may exhibit more complex gas kinematics potentially accessible through observations: beyond the non-axisymmetric features dominated by planets, magnetic fields cause both radial and vertical motions of the gas to extend beyond the vicinity of the planet, and the directions of these movements are no longer solely dependent on gravitational forces and pure hydrodynamic effects like the pressure gradient.

Comparing our findings with those of Aoyama & Bai (2023) and Wafflard-Fernandez & Lesur (2023), we note a similar emphasis on the significant role of magnetized disk winds and the concentration of the poloidal magnetic flux in the gap. Among the three asymmetries of gap layout in Wafflard-Fernandez & Lesur (2023), we did not find notable radial width asymmetry or radial depth asymmetry. In the azimuthal direction, our results also demonstrate asymmetries that, while not drastic, are still relatively significant. During the early stages of gap opening, there is a relatively higher surface density on the side of the planet's leading edge, which may be associated with the lower magnetic field line density observed in this region as illustrated in Figure 10; a weaker magnetic field on this side reduces the accretion rate. After $t=80 \tau_p$, the high-density region shifts to the trailing edge side. By $t=90 \tau_p$, this area shrinks to within $\pi/4$. This region remains stable until $t=110 \tau_p$, after which there is a tendency for it to shift back towards the leading edge side.

Our work distinguishes itself by utilizing the magnetic diffusion lookup table from Hu et al. (2023), allowing for a more detailed and accurate depiction of magnetic diffusion processes within the disk. This approach enables us to capture the complex feedback mechanisms between disk magnetization, wind properties, and planet-induced structures that were not fully addressed by the fixed ambipolar Elsasser number (Am) profiles used in the aforementioned studies. Several features are unique in our simulations due to this diffusion profile.

First, spontaneous symmetry breaking could stem from the vertical stratification of magnetic diffusion inside the disk. In tests without a planet, we found that asymmetry begins to emerge after just $20 \tau_p$, even leading to scenarios

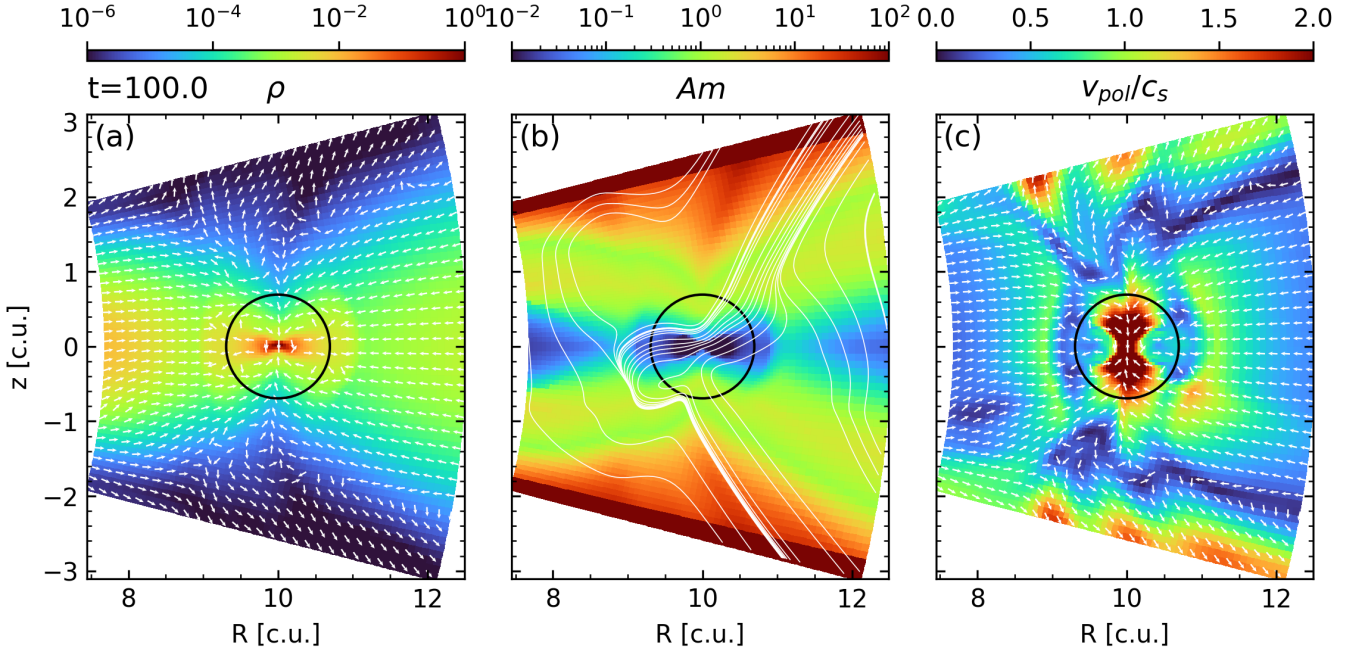


Figure 16. Azimuthally averaged gas properties around the planet, within the 8 cells along ϕ direction. Panel (a): gas density (in code units) with white arrows representing velocity vectors in the poloidal plane; (b): ambipolar Elsasser number and poloidal magnetic fields (solid white lines); (c): poloidal velocity divided by the local sound speed with white arrows representing velocity vectors in the poloidal plane. The solid black circle in each panel shows the planet’s Hill sphere. See the supplementary online material for an animated version of this figure.

where disk winds occur on only one side. The planet torque is a perturber with mirror symmetry to the midplane, thus it could potentially help the disk maintain symmetry. The planet-free spontaneous symmetry breaking has also been confirmed by linear theory (Wang et al. 2024). The one-sided accretion layer in our simulation is already formed in the outer disk. This is different from the accretion stream in Wafflard-Fernandez & Lesur (2023) (see their Fig.7 and Fig.A.1), where it enters the gap through the midplane and is only slightly biased towards the bottom of the disk. This is because a constant lower Elsasser number ($Am = 1$) was used inside the disk, leading to accretion dominated by the densest midplane. In addition, the fixed Am in Wafflard-Fernandez & Lesur (2023) is not completely unchanged because it has a lower limit that depends on the ratio of Alfvén velocity and sound speed (v_a/c_s), which, in the gap, due to reduced density and increased magnetic field strength, locally decreases the diffusion strength, with a corresponding increase in Am .

Second, the stronger magnetic diffusion outside the gap in our simulation maintains a more laminar disk. For example, in Model $3M_j\beta_3$ (3 Jupiter-mass planet, with disk’s initial midplane plasma $\beta = 10^3$) of Wafflard-Fernandez & Lesur (2023), the flow field within the disk exhibits a high degree of temporal variability, with the position and shape of large vortices changing significantly within one or two local orbits. In contrast, our accretion stream and vortex remained stable longer (greater than 20). The MRI active disk in Aoyama & Bai (2023) is also highly dynamic and pro-

duces planet-free magnetic flux concentration that drives a second gap inside the planetary orbit.

Although the look-up table is a step forward over fixed diffusion profiles, several caveats are worth mentioning. As mentioned in Section 3.3, the look-up table may be unreliable in high-density regions such as the CPD. This limitation arises not only from the CPD’s density exceeding initial values but also from inaccuracies in ionization estimates. The second parameter, vertical location, aims to capture the complex effects of varied ionization sources. Near the midplane, ionization is dominated by diffusion sources, including down-scattered X-ray photons, cosmic rays, and short-lived radionuclides. Furthermore, hard X-ray photons from the central star may penetrate 1-2 scale heights below the disk surface. In the original 2D simulation, diffuse ionization attenuation was calculated using column density derived from the local density and scale height. Given the CPD’s smaller scale height compared to the protoplanetary disk (PPD), this may lead to an overestimated attenuation. Apart from these microphysics processes, the gap morphology in the 2D simulation differs somewhat from 3D. In particular, the 2D simulation does not capture non-axisymmetric structures like spiral shocks and the CPD. The look-up table is constructed from the diffusion profile at the gap center, encompassing the widest density range. However, the behavior at the gap edge may differ. Future improvements should incorporate radial variations in the look-up table to enhance its reliability across the gap region.

The fast accretion layer across the gap is reminiscent of the dust conveyor belt in Hu et al. (2022). The layer repre-

sents a stable gas feature resulting from efficient magnetic braking associated with the toroidal magnetic field reversal. It serves a dual role as both a trap and a conveyor for dust grains. These grains rapidly migrate inward, driven by gas advection and their inherent radial drift. Interestingly, the dust grains do not congregate at the density peaks within the gas rings, a scenario one might expect if the pressure-gradient driven radial drift were the dominant factor in dust aggregation. Rather, they are primarily found in the inner portions of these rings, where the gas rotation velocity surpasses the local Keplerian speed. This pattern suggests that the dust dynamics are more significantly impacted by the overall gas motions than by the pressure gradients. Similar meridional circulation patterns also occur in the vicinity of the planet-opened gap and the outer gap edge. The accretion layer is expected to similarly transport dust grains across the pressure maximum at the gap edge. However, since the accretion layer is concentrated on one side of the midplane, it may be less efficient in transporting settled larger grains than smaller grains. On the other hand, both the planet and magnetic fields induce significant vertical motions within the disk, facilitating the lifting of more grains from the midplane into the accretion layer. Adding the third dimension, the “shrunk” horseshoe orbit forms a vortex between the planet and the trailing Lagrangian point L5. The overdensity is located in the same area but can slowly shift to the other side of the planet. Dust clumps near L4 and L5 have been observed in LkCa 15 disk (Long et al. 2022). Note the overdensity is seen at the leading side of the planet in hydro simulations with wind torque (Kimmig et al. 2020), and the MHD disk in Wafflard-Fernandez & Lesur (2023) showed a similar oscillation of mass distribution along the azimuthal dimension. This indicates that under the combined influence of magnetic fields, disk wind, and accretion streams, the low-density horseshoe region could exhibit unprecedentedly complex behavior. It would be interesting to explore the dust dynamics and distribution near planet-opened gaps in non-ideal MHD disks quantitatively in the future.

In summary, we have carried out a 3D simulation of the gap opening by an embedded planet in a non-ideal MHD disk using magnetic diffusivities from a published axisymmetric simulation with consistent thermochemistry. The main results are as follows:

- We find a strong concentration of the poloidal magnetic flux in the planet-opened gap (see Figures 2b and 8b), in agreement with previous work. In our simulation, the mass depletion by the embedded planet makes the low-density gap region better coupled to the magnetic field than the bulk of the disk material outside the gap (see Figure 8b).
- The relatively strong magnetic field and good field-matter coupling enable efficient magnetic braking of the gap material, driving a fast accretion layer that is significantly displaced from the disk midplane (see Figure 8e). The accretion layer is located where the field lines bend most in the radial (see Figure 8b) and azimuthal (see Figure 10b) directions. Its angular momentum removal is dominated by the $z\phi$ -component of the Maxwell stress (see Figure 5).
- The magnetically driven fast accretion helps deplete the gap at late times compared to the non-magnetic (hydro) case (see Figure 7b). This magnetically driven mass depletion reduces the mass reservoir in the circumplanetary en-

vironment and is expected to negatively impact the growth of the planet (see Figure 7a). In the fast accretion layer, the region of horseshoe orbits on the trailing side of the planet is greatly reduced (see Figure 11), which is expected to impact the corotation torque on the planet.

- The poloidal gas kinematics in the gap is dominated by an interplay between the magnetically driven disk wind and magnetically driven fast accretion layer that, in our simulation, is displaced below the midplane. Sandwiched between the disk wind from the top surface and the fast accretion layer below the midplane is a large, persistent vortex that dominates the gas kinematics in the meridional plane (see Figure 9). The meridional vortex in the gap may be observable as a redshifted (or blueshifted, depending on the disk inclination) ring (see Figure 12). The fast accretion layer may also be observable if located close enough to the surface.

ACKNOWLEDGEMENTS

We thank the referee for a detailed constructive report that improved the presentation of the paper. ZYL is supported in part by NASA 80NSSC20K0533 and NSF AST-2307199. Our simulations are made possible by an XSEDE allocation (AST200032). Z.Z. acknowledges support from the National Science Foundation under CAREER Grant Number AST-1753168 and support from NASA award 80NSSC22K1413. Figures in this paper were made with the help of `Matplotlib` (Hunter 2007) and `NumPy` (Harris et al. 2020). `cblind` is also used in one of the colormaps.

DATA AVAILABILITY

The data from the simulations will be shared on reasonable request to the corresponding authors.

REFERENCES

- ALMA Partnership et al., 2015, *ApJ*, 808, L3
 Andrews S. M., 2020, *ARA&A*, 58, 483
 Aoyama Y., Bai X.-N., 2023, *ApJ*, 946, 5
 Bae J., et al., 2022, *ApJ*, 934, L20
 Bae J., Isella A., Zhu Z., Martin R., Okuzumi S., Suriano S., 2023, in Inutsuka S., Aikawa Y., Muto T., Tomida K., Tamura M., eds, *Astronomical Society of the Pacific Conference Series Vol. 534, Protostars and Planets VII*. p. 423 ([arXiv:2210.13314](https://arxiv.org/abs/2210.13314)), [doi:10.48550/arXiv.2210.13314](https://doi.org/10.48550/arXiv.2210.13314)
 Bai X.-N., Stone J. M., 2017, *ApJ*, 836, 46
 Baruteau C., Fromang S., Nelson R. P., Masset F., 2011, *A&A*, 533, A84
 Baruteau C., et al., 2014, in Beuther H., Klessen R. S., Dullemond C. P., Henning T., eds, *Protostars and Planets VI*. pp 667–689 ([arXiv:1312.4293](https://arxiv.org/abs/1312.4293)), [doi:10.2458/azu'uapress'9780816531240-ch029](https://doi.org/10.2458/azu'uapress'9780816531240-ch029)
 Béthune W., Lesur G., Ferreira J., 2017, *A&A*, 600, A75
 Carballido A., Matthews L. S., Hyde T. W., 2017, *MNRAS*, 472, 3277
 Crida A., Morbidelli A., Masset F., 2006, *Icarus*, 181, 587
 Cui C., Bai X.-N., 2021, *MNRAS*, 507, 1106
 Dullemond C. P., Juhasz A., Pohl A., Sereshi F., Shetty R., Peters T., Commercon B., Flock M., 2012, *RADMC-3D: A*

- multi-purpose radiative transfer tool, Astrophysics Source Code Library, record ascl:1202.015
- Elbakyan V., Wu Y., Nayakshin S., Rosotti G., 2022, *MNRAS*, **515**, 3113
- Fang M., et al., 2023, *Nature Astronomy*, **7**, 905
- Fung J., Chiang E., 2016, *ApJ*, **832**, 105
- Galloway-Sprietsma M., et al., 2023, *ApJ*, **950**, 147
- Gonzalez J. F., Laibe G., Maddison S. T., 2017, *MNRAS*, **467**, 1984
- Gressel O., Nelson R. P., Turner N. J., Ziegler U., 2013, *ApJ*, **779**, 59
- Harris C. R., et al., 2020, *Nature*, **585**, 357
- Hu X., Zhu Z., Okuzumi S., Bai X.-N., Wang L., Tomida K., Stone J. M., 2019, *ApJ*, **885**, 36
- Hu X., Wang L., Okuzumi S., Zhu Z., 2021, *ApJ*, **913**, 133
- Hu X., Li Z.-Y., Zhu Z., Yang C.-C., 2022, *MNRAS*, **516**, 2006
- Hu X., Li Z.-Y., Wang L., Zhu Z., Bae J., 2023, *MNRAS*, **523**, 4883
- Huang J., et al., 2018, *ApJ*, **869**, L42
- Hunter J. D., 2007, *Computing in Science & Engineering*, **9**, 90
- Izquierdo A. F., Testi L., Facchini S., Rosotti G. P., van Dishoeck E. F., 2021, *A&A*, **650**, A179
- Izquierdo A. F., Testi L., Facchini S., Rosotti G. P., van Dishoeck E. F., Wölfer L., Paneque-Carreño T., 2023, *A&A*, **674**, A113
- Kimmig C. N., Dullemond C. P., Kley W., 2020, *A&A*, **633**, A4
- Kley W., D'Angelo G., Henning T., 2001, *ApJ*, **547**, 457
- Law C. J., et al., 2021, *ApJS*, **257**, 4
- Lega E., Morbidelli A., Nelson R. P., Ramos X. S., Crida A., Béthune W., Batygin K., 2022, *A&A*, **658**, A32
- Lesur G. R. J., 2021, *A&A*, **650**, A35
- Lin D. N. C., Papaloizou J. C. B., 1993, in Levy E. H., Lunine J. I., eds, *Protostars and Planets III*. p. 749
- Long F., et al., 2022, *ApJ*, **937**, L1
- Masset F., 2000, *Astronomy and Astrophysics Supplement Series*, **141**, 165
- Miranda R., Rafikov R. R., 2019, *ApJ*, **875**, 37
- Nelson R. P., Papaloizou J. C. B., 2003, *MNRAS*, **339**, 993
- Öberg K. I., et al., 2021, *ApJS*, **257**, 1
- Ogihara M., Morbidelli A., Guillot T., 2015, *A&A*, **584**, L1
- Ogihara M., Kokubo E., Suzuki T. K., Morbidelli A., Crida A., 2017, *A&A*, **608**, A74
- Okuzumi S., Momose M., Sirono S.-i., Kobayashi H., Tanaka H., 2016, *ApJ*, **821**, 82
- Paardekooper S. J., Baruteau C., Crida A., Kley W., 2010, *MNRAS*, **401**, 1950
- Paneque-Carreño T., Miotello A., van Dishoeck E. F., Tabone B., Izquierdo A. F., Facchini S., 2023, *A&A*, **669**, A126
- Pinte C., et al., 2020, *ApJ*, **890**, L9
- Riols A., Lesur G., Menard F., 2020, *A&A*, **639**, A95
- Stone J. M., Tomida K., White C. J., Felker K. G., 2020, *ApJS*, **249**, 4
- Suriano S. S., Li Z.-Y., Krasnopolsky R., Shang H., 2017, *MNRAS*, **468**, 3850
- Suriano S. S., Li Z.-Y., Krasnopolsky R., Shang H., 2018, *MNRAS*, **477**, 1239
- Tabone B., Rosotti G. P., Cridland A. J., Armitage P. J., Lodato G., 2022, *MNRAS*, **512**, 2290
- Teague R., 2019, *The Journal of Open Source Software*, **4**, 1220
- Teague R., Bae J., Bergin E. A., 2019, *Nature*, **574**, 378
- Teague R., et al., 2021, *ApJS*, **257**, 18
- Wafflard-Fernandez G., Lesur G., 2023, *A&A*, **677**, A70
- Wang L., Bai X.-N., Goodman J., 2019, *ApJ*, **874**, 90
- Wang L., Xu S., Wang Z., Fang M., Goodman J., 2024, *ApJ*, **972**, 142
- Winters W. F., Balbus S. A., Hawley J. F., 2003, *ApJ*, **589**, 543
- Wu Y., Chen Y.-X., Jiang H., Dong R., Macías E., Lin M.-K., Rosotti G. P., Elbakyan V., 2023, *MNRAS*, **523**, 2630
- Zanni C., Ferrari A., Rosner R., Bodo G., Massaglia S., 2007, *A&A*, **469**, 811
- Zhang K., Blake G. A., Bergin E. A., 2015, *ApJ*, **806**, L7
- Zhang K., et al., 2021, *ApJS*, **257**, 5
- Zhu Z., Stone J. M., Rafikov R. R., 2013, *ApJ*, **768**, 143

This paper has been typeset from a $\text{\TeX}/\text{\LaTeX}$ file prepared by the author.